

## Characterization of a hybrid array of single and multi-absorber transition-edge sensor microcalorimeters for the Line Emission Mapper

Nicholas Wakeham<sup>a,b,\*</sup> Joseph S. Adams,<sup>a,b</sup> Simon R. Bandler,<sup>b</sup>  
James A. Chervenak,<sup>b</sup> Renata S. Cumbee,<sup>b</sup> Fred M. Finkbeiner<sup>b,c</sup>  
Joshua Fuhrman<sup>a,b</sup> Samuel Hull,<sup>b,d</sup> Richard L. Kelley,<sup>b</sup> Caroline A. Kilbourne<sup>b</sup>,  
Kazuhiro Sakai<sup>a,b</sup> Stephen J. Smith<sup>b</sup> Edward J. Wassell,<sup>b</sup> and Sang Yoon<sup>b,e</sup>

<sup>a</sup>University of Maryland, Center for Space Sciences and Technology, Baltimore, Maryland, United States

<sup>b</sup>NASA Goddard Space Flight Center, Greenbelt, Maryland, United States

<sup>c</sup>Sigma Space Corp./Hexagon US Federal, Lanham, Maryland, United States

<sup>d</sup>University of Maryland, Department of Astronomy, College Park, Maryland, United States

<sup>e</sup>Science Systems and Applications, Inc., Lanham, Maryland, United States

**ABSTRACT.** The Line Emission Mapper (LEM) is a proposed x-ray probe mission to study the physics of galaxy formation through spectral and spatial measurements of x-rays in the energy band of 0.2 to 2 keV. The LEM Microcalorimeter Spectrometer instrument on LEM will have a hybrid transition-edge sensor (TES) microcalorimeter array made up of an inner array of single-pixels with one x-ray absorber connected to one TES and an outer array of multi-absorber microcalorimeters, or “hydras,” with four absorbers connected to a single TES, each with a different thermal conductance. Here, we characterize the first hybrid array of single-pixel and multi-absorber microcalorimeters designed for LEM. We present the fundamental transition, noise, and detector performance properties to demonstrate their suitability for the mission. We also show that the spectral resolution at the  $\text{AlK}_\alpha$  line is  $1.92 \pm 0.02$  eV for the 4-pixel hydra (coadded) and  $0.90 \pm 0.02$  eV for the single-pixels. This is significantly better resolution than the LEM mission level requirement. Finally, we demonstrate that the position discrimination between the four pixels of the hydra can be achieved down to 200 eV when measured with a time-division multiplexed readout using timings representative of the anticipated LEM requirements.

© The Authors. Published by SPIE under a Creative Commons Attribution 4.0 International License. Distribution or reproduction of this work in whole or in part requires full attribution of the original publication, including its DOI. [DOI: [10.1117/1.JATIS.9.4.041006](https://doi.org/10.1117/1.JATIS.9.4.041006)]

**Keywords:** detectors; detector arrays; calorimetry; spectrometers; x-rays

Paper 23080SS received Jul. 20, 2023; revised Oct. 5, 2023; accepted Oct. 6, 2023; published Oct. 20, 2023.

### 1 Introduction

The Line Emission Mapper (LEM) is an x-ray observatory satellite proposed for launch in the 2030s. The main purpose of LEM is to study the physics of the formation of galaxies and, in particular, the diffuse gas in the Circumgalactic Medium and Intergalactic Medium.<sup>1</sup> To achieve this, LEM is proposed to have a 30' field of view with 18" angular resolution, with the LEM Microcalorimeter Spectrometer (LMS) as the detector instrument at its core. The LMS will have an array of transition-edge sensor (TES) microcalorimeters optimized for measurement in the 0.2 to 2 keV energy band. There will be an inner region of the array with 784 pixels capable of 1.3 eV resolution at 1 keV and an outer region of 12,736 pixels capable of 2.5 eV at 1 keV.

\*Address all correspondence to Nicholas Wakeham, [nicholas.a.wakeham@nasa.gov](mailto:nicholas.a.wakeham@nasa.gov)

To read out  $\sim 14$  kilo-pixels within the constraints of mass and power of a satellite mission requires large multiplexing factors. The inner region will have an array of  $15''$  pixels ( $290 \mu\text{m}$  pixel pitch), each with a single x-ray absorber pixel connected to a single TES. These single-pixels will be read out using time-division multiplexing (TDM) with 60 timing rows. The outer region will have 3184 TESs, also read out with 60 row TDM, but additionally each TES will connect to four  $15''$  x-ray absorber pixels to give a total of  $3184 \times 4 = 12,736$  pixels. In such a multi-absorber TES microcalorimeter, or “hydra,” the position sensitivity between the four absorbers is achieved by each absorber having a different thermal conductance to the TES. Thus, the position discrimination can be determined through analysis of the x-ray pulse-shape.<sup>2,3</sup>

The development of single-pixel and hydra TES microcalorimeters has been an area of intense study over the last several decades,<sup>4,5</sup> and in particular it has been developed for potential space-based astrophysics applications, such as Lynx,<sup>3,6</sup> Constellation-X,<sup>7,8</sup> and ATHENA.<sup>9–13</sup> LEM places a unique combination of constraints on the TES microcalorimeter design but draws upon knowledge from the designs and prototype arrays of each of these missions. The ATHENA X-IFU design has a pixel pitch of  $317 \mu\text{m}$ , similar to LEM’s  $290 \mu\text{m}$ , with a similar total number of TES pixels. However, the X-IFU array is designed with only single-pixels and is optimized for 7 keV with a range of 0.3 to 12 keV. Constellation-X was designed with a hybrid array of single-pixels and hydras, but again for higher energies than LEM and higher count rate requirements. The Lynx mission was also designed with a hybrid array of single-pixels and hydras, with regions optimized for different observations. The hydras in the main array and enhanced main array for Lynx have 25 absorbers per TES and were designed for an energy range up to 7 keV. The ultra high resolution array on Lynx was designed with single-pixels for energies up to 0.75 keV. The pixels in Lynx have a much smaller pixel pitch than LEM of 25 to  $50 \mu\text{m}$ .

The knowledge gained from these previous mission prototypes has been applied to design TES microcalorimeters optimized for the LEM mission. In recent years, there have also been considerable advances in the understanding of the TES superconducting transition,<sup>14–16</sup> noise,<sup>17–19</sup> and energy gain scale properties,<sup>20</sup> as well as their optimization for TDM readout.<sup>12,21</sup> Advances in TDM readout of TES microcalorimeters in the last few years show that the noise levels and band width required for 60 row TDM of LEM pixels will be achievable,<sup>22,23</sup> but this will be experimentally demonstrated in the near future.

In this report, we present characterization of the first hybrid array of single-pixels and hydras designed for LEM. Through measurement of the TES transition and x-ray performance properties, we show that these pixels are well suited to this application. Section 2 shows the detailed TES design and the electro-thermal models used to describe the single-pixels and hydras. Section 3 presents the results of characterization of the TES transition properties, pixel performance, and position sensitivity of the hydra designs when read out using representative timing of 60 row TDM. These results are then discussed in relation to the LEM requirements and future demonstrations in Sec. 4.

## 2 Methods

### 2.1 Pixel Design

Figure 1 shows an image of a kilo-pixel hybrid array designed as a demonstration for LEM and used in this study. The chip has a central array of 256 single-pixels with 192 4-pixel hydras around it. The measurements reported here were performed on several single-pixels and hydras in the top left quadrant of the array with a uniform TES design.

#### 2.1.1 Single-pixel

The design of the single-pixels is shown in Fig. 2. The TES Mo/Au bilayer is  $47/300 \text{ nm}$  thick, has a sheet resistance  $R_{\square} = 9 \text{ m}\Omega/\square$ , and is  $50 \mu\text{m}$  long in the current direction and  $15 \mu\text{m}$  wide. Au banks run down each edge of the TES parallel to the current direction. They are each  $6 \mu\text{m}$  wide, overlap the bilayer by  $3 \mu\text{m}$ , and have a low temperature sheet resistance of  $20 \text{ m}\Omega/\square$ . The TES is at the center of a square region of silicon nitride behind which the Si chip has been etched away. This ensures that the thermal conduction from the TES to the thermal bath of the Si chip is through the relatively low thermal conductance of the  $0.5 \mu\text{m}$  thick

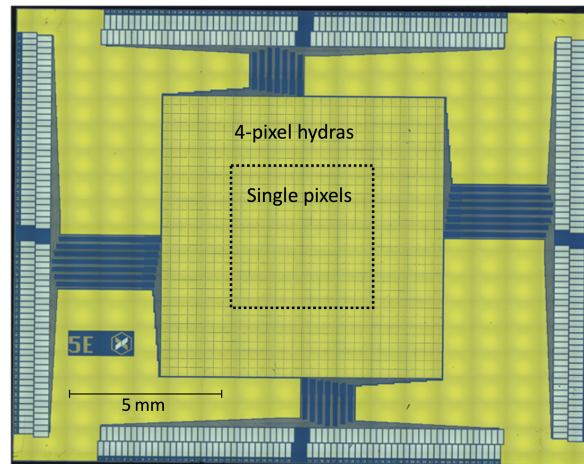


**Fig. 1** Photograph of a kilo-pixel hybrid array chip. It contains a center array of single-pixels, with one absorber connected to a single TES, and an outer array of 4-pixel hydras, with four absorbers connected to a single TES.

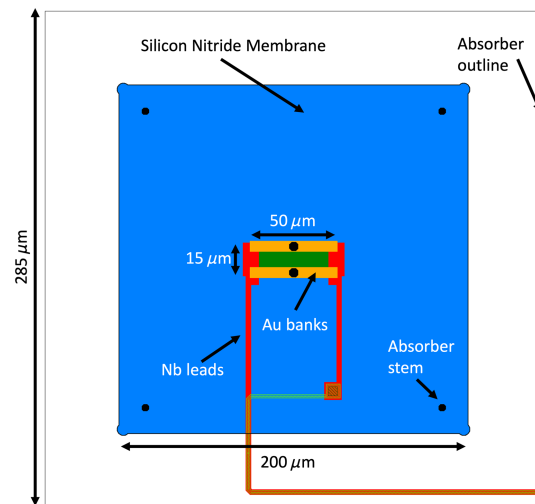


**Fig. 2** Diagram of the single-pixel design.

silicon nitride. The electrical connection to the TES is made using Nb wires that overlap the bilayer by  $5 \mu\text{m}$  at each end. A square Au x-ray absorber is supported  $\sim 4 \mu\text{m}$  above the plane of the TES by six cylindrical Au pillar absorber stems. Four of these are placed on the silicon nitride and have a diameter of  $4 \mu\text{m}$ , and two are placed on the Au banks of the TES and have a diameter of  $5 \mu\text{m}$ . The stems and absorber have a low temperature resistivity of  $\sim 1 \text{ n}\Omega\text{m}$ . The pixel pitch is  $290 \mu\text{m}$  and the side length of the absorber is  $285 \mu\text{m}$  with a thickness of  $0.52 \mu\text{m}$ .

### 2.1.2 Hydra

The design of the hydras is shown in Fig. 3. The absorber size is the same as the single-pixel design, but four absorbers connect to one TES at the center. The TES design for the hydras is very similar to that of the single-pixels. The Mo/Au bilayer is  $50 \mu\text{m}$  long and  $15 \mu\text{m}$  wide, with Nb leads at either end. The Au banks in this case run beyond the length of the bilayer to allow for thermal connection to the absorbers through Au links placed on the silicon nitride membrane and connected to one stem of an absorber and the banks. These links are a different length for each pixel of the hydra to give a different thermal conductance between the TES and the absorber, which allows for the position discrimination of x-ray pulses in each of the pixels. The low temperature sheet resistance of the links is  $20 \text{ m}\Omega/\square$ . The pixel number is shown in the corner of

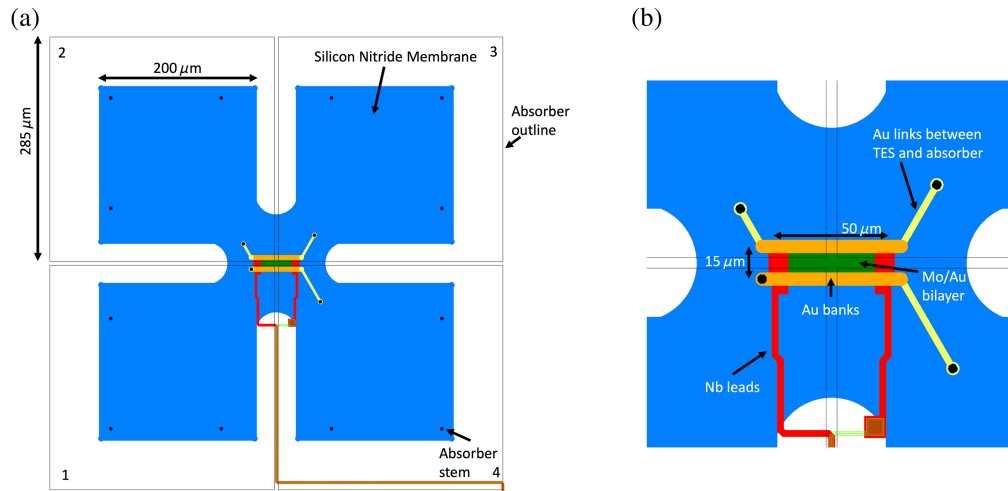


**Fig. 3** (a) Diagram of 4-pixel hydra design and (b) zoom in of the TES design. Pixel number is indicated by the number in the corner of each absorber.

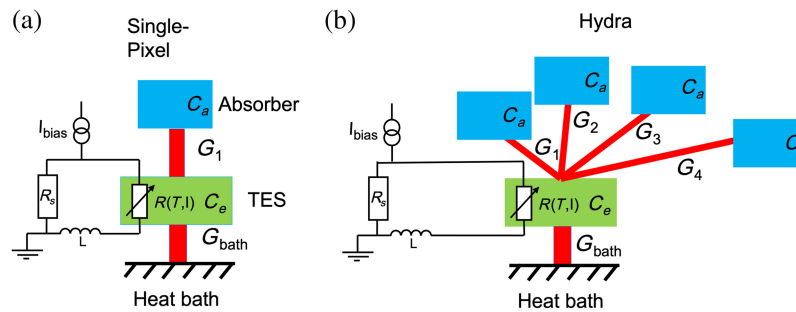


**Fig. 4** Schematic diagram of the electro-thermal model of (a) single-pixels and (b) hydras. Adapted from Ref. 17.

each absorber in Fig. 3(a). Pixel 1 has no link, so the absorber stem sits directly on the bank. Each absorber is supported by three other stems toward the edge of the silicon nitride membrane. All stems have a diameter of  $4 \mu\text{m}$ .

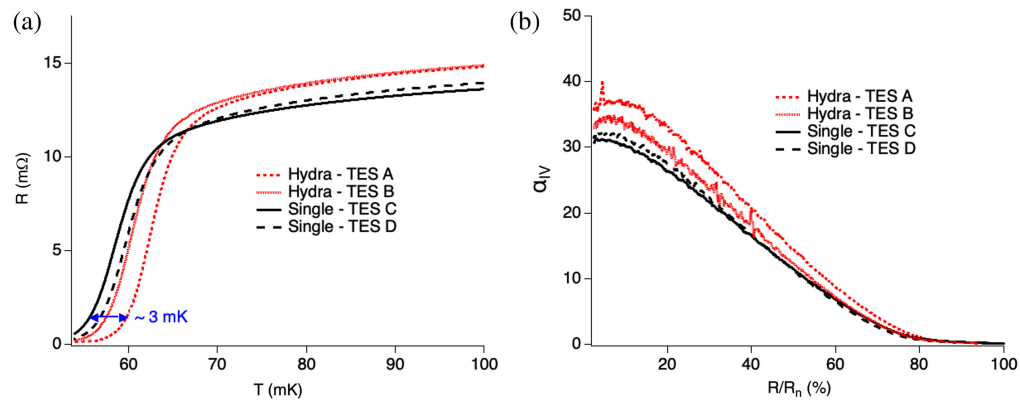
## 2.2 Electro-Thermal Models

Figure 4(a) shows the two-body electro-thermal model of a microcalorimeter that has previously been used to describe the noise characteristics of Mo/Au TESs.<sup>17</sup> In this model, the TES, with heat capacity  $C_e$ , is thermally connected to an absorber, with heat capacity  $C_a$ , by thermal conductance  $G_1$ . The TES is also thermally connected to the heat bath by thermal conductance  $G_{\text{bath}}$ . This model is used here to understand the behavior of the single-pixels. To describe the hydras, we extended this model to include four absorbers, all with the same heat capacity  $C_a$  but with a different thermal conductance  $G_x$  between the absorber of pixel  $x$  and the TES. The TES circuit is also shown in Fig. 4, where the variable resistor represents the TES with resistance  $R$ , which varies as a function of TES temperature  $T$  and TES current  $I$ . The shunt resistor  $R_s$  and additional inductor  $L$  are also shown.

## 3 Results

### 3.1 Transition Properties

Figure 5(a) shows the TES resistance  $R$  as a function of the TES temperature  $T$  for two four-pixel hydras (TES A and B) and two single-pixels (TES C and D) sampled across one quadrant of the array. Out of the total of five hydras and seven single-pixels measured in the quadrant, these four were selected as suitably representative for further study because they span the measured range of



**Fig. 5** (a) Resistance  $R$  as a function of TES temperature  $T$  for two single-pixels and two hydras. (b)  $\alpha_{IV} = \frac{T}{R} \frac{dR}{dT}$  as a function of  $R$  as fraction of normal state resistance  $R_n$ . Double headed arrow shows spread in  $T_c$ .

transition temperature and normal resistance.  $R(T)$  was calculated from the measurement of  $I$  as a function of TES bias voltage  $V_{\text{bias}}$  and the thermal conductance from the pixel to the thermal bath  $G_{\text{bath}}$  for each pixel.  $G_{\text{bath}}$  was calculated from fitting TES power as a function of heat bath temperature  $T_{\text{bath}}$  at a bias point in the transition of  $R/R_n = 90\%$ , where  $R_n$  is the normal state resistance of the TES. Calculating  $G_{\text{bath}}$  at this large value of  $R/R_n$  has been shown to be more accurate for small TESs.<sup>24,25</sup> From these measurements, we calculate  $G_{\text{bath}}(T_c) = 21$  pW/K and 48 pW/K for the single-pixel and hydra, respectively, where  $T_c$  is defined as  $T$  at  $R/R_n = 10\%$ . The approximately two times larger  $G_{\text{bath}}$  in the hydra compared with the single-pixel is expected because the larger banks, additional Au links, and increased number of absorber stems mean that there is an approximately two times larger phonon emitting perimeter.  $G_{\text{bath}}$  has been shown to be proportional to this perimeter when limited by ballistic phonon transport.<sup>26–29</sup> Figure 5(a) shows that the average  $T_c$  is around 58 mK, which is within the target for LEM of 55 to 60 mK. There is a small spread in the transition temperature  $T_c$  of around 3 mK between the different TESs. A variation of a few mK is typically seen across an array of this size from non-uniformity in the Mo/Au bilayer properties resulting from fabrication, but this may be improved in the future with better bilayer thickness uniformity. The normal state resistance of the TESs of the two single-pixels are consistent with each other, as are the two TESs on the hydras, but  $R_n$  of the single-pixels is smaller than that of the hydras by  $\sim 5\%$ . This is consistent with the predicted effect of the reduced resistance of the gold banks in the single-pixels because of the thick gold absorber stems in the center, as shown in Fig. 2. These stems are at the ends of the banks in the hydra design, as shown in Fig. 3(b), and therefore do not reduce the resistance of the current path along the banks in that case. Figure 5(b) shows  $\alpha_{IV} = \frac{T}{R} \frac{dR}{dT}$  calculated from Fig. 5(a).  $\alpha_{IV}$  appears to be higher in the hydra pixels; however, the difference is small, and more measurements of many pixels will be needed to determine if this is a significant difference between the designs.

Further information about the TES transition properties was obtained from measurements of the complex impedance of the TES from 10 Hz to 5 kHz. The details of these measurements are described elsewhere.<sup>17,30,31</sup> To extract the transition parameters, the complex impedance measurements were fitted using the single-pixel and hydra models described in Sec. 2.2. Measured values of  $G_{\text{bath}}$ ,  $R$ ,  $T$ , and  $R_{\text{shunt}}$  were used in the model. The total heat capacity at  $T_c$  was calculated from literature values of the specific heat and the volume of all component parts of the pixels. It was then increased by  $\sim 10\%$  to 0.21 pJ/K and 0.90 pJ/K in the single-pixel and hydra, respectively, to allow for a better fit to the complex impedance. The thermal conductance between the absorber of the single-pixel (or pixel 1 of the hydra) and the TES  $G_1$  was estimated from the normal state sheet resistance of the TES bilayer using the Wiedemann–Franz law to be 91 nW/K at  $T_c$ . This approximation has been shown to give a reasonable order of magnitude estimate in other Mo/Au TESs, with or without Au banks.<sup>17,32</sup> The thermal conductance of the stems and absorber are large enough to be negligible. The thermal conductance between the absorbers of pixels 2 to 4 in the hydra were also estimated from the Wiedemann–Franz law, using the measured sheet resistance and geometry of the Au links and then adding the sheet

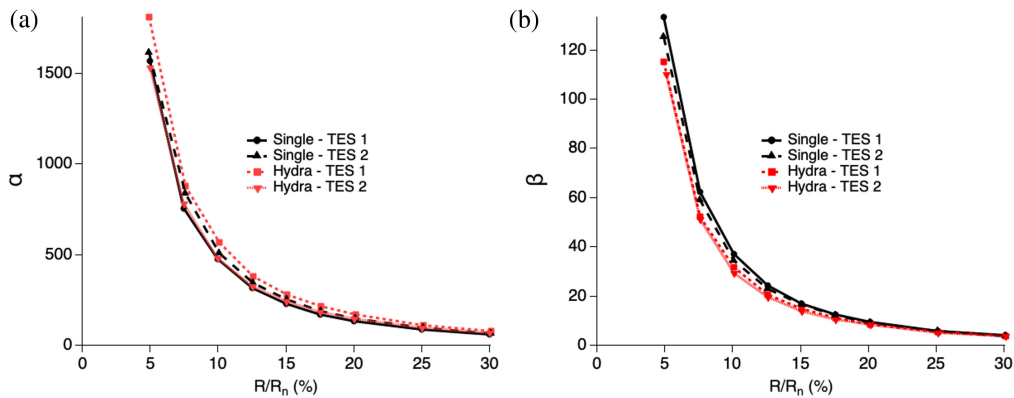


**Fig. 6** TES transition parameters (a)  $\alpha = (T/R)\partial R/\partial T|_I$  and (b)  $\beta = (I/R)\partial R/\partial I|_T$  as a function of  $R/R_n$ .

resistance of the TES bilayer in series. This gives  $G_2$ ,  $G_3$ , and  $G_4$  as 9.5, 6.1, and 4.3 nW/K at  $T_c$ , respectively. Figure 6(a) shows  $\alpha = (T/R)\partial R/\partial T|_I$  and Fig. 6(b) shows  $\beta = (I/R)\partial R/\partial I|_T$  as a function of  $R/R_n$ . As seen in other Mo/Au TES designs with a length of 50  $\mu\text{m}$ ,<sup>27,33</sup>  $\alpha$  and  $\beta$  decrease rapidly with increasing  $R/R_n$ . There is no significant variation in  $\alpha$  between the hydra and single-pixel designs. The  $\beta$  appears lower in the hydra designs, which is consistent with the larger  $\alpha_{IV}$ , but, again, determining whether this is an intrinsic difference between the designs will require further investigation of a large sample of pixels.

### 3.2 Pixel Performance

Next, we investigated the noise, x-ray pulse-shape properties, energy resolution, and energy gain scale sensitivities of each pixel design. These are all key properties for the design of the LMS instrument on the LEM mission, and they provide input to determine what instrument performance will be achievable. These measurements predominantly focused on the bias point  $R/R_n = 10\%$  because this has been shown in devices optimized for X-IFU to be a good compromise of spectral resolution and pixel speed.<sup>11</sup> However, we will also discuss whether this choice may be further refined in the future.

#### 3.2.1 Noise

Figure 7 shows the measured current noise in the single-pixel and hydra at  $R/R_n = 10\%$ . The noise for each type was fitted using the single-pixel or hydra model described in Sec. 2.2 and Sec. 3.1 and in more detail in Ref. 17. The readout noise was assumed to be white and was measured with the TES in the superconducting state and at sufficiently high frequency to not be influenced by noise from the TES circuit.

In contrast to higher resistance Mo/Au devices, for these devices, the internal thermal fluctuation noise  $a_x$  between the absorber(s) and TES (where  $x$  is the pixel number) was not sufficient to account for the total observed noise at intermediate frequencies.<sup>17</sup> Therefore, as is common practice for TESs, the Johnson noise term  $J_{\text{TES}}$  was increased by a factor of  $\sqrt{1 + M^2}$  to fit the data. An  $M^2$  value of 3.9 was used in the single-pixel and 3.5 in the hydra. It was shown recently that this excess Johnson noise may be the result of Johnson noise that is ‘mixed-down’ from a higher frequency by Josephson oscillations in TESs with a non-linear current-voltage relationship.<sup>18,19</sup> Attempting to fit to that model would require significantly more measurements and is beyond the scope of this work, but the reasonable agreement between the  $M^2$  value needed in these two TESs with similar transition properties, but very different thermal properties, is consistent with an electrical origin, such as ‘‘mixed-down’’ Johnson noise. As noted on previous devices,<sup>2,17,34</sup> the thermal fluctuation noise term between the TES and thermal bath  $P_{\text{bath}}$  must also be increased from the theoretical prediction to account for the measured noise at the lowest frequency. The origin of the  $\sim 30\%$  increase in  $P_{\text{bath}}$  in the single-pixel and 45% increase in the hydra case observed here is not understood, but it may be the result of additional complexity in the thermal system not accounted for in the simplified discrete model described above. This

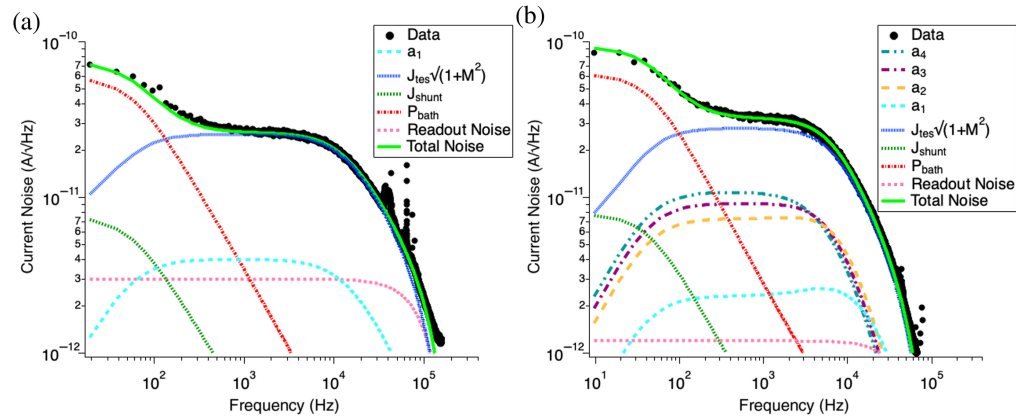


**Fig. 7** Measured and calculated current noise as a function of frequency for (a) single-pixel and (b) hydra.  $T_{\text{bath}} = 40$  mK, and TES was voltage biased at  $R/R_n = 10\%$ . Noise was fitted using the models described in Sec. 2.2. Term  $a_x$  is the internal thermal fluctuation noise between the absorber of pixel  $x$  and the TES.  $J_{\text{tes}}$  is the TES non-equilibrium Johnson noise increased by a factor of  $\sqrt{1 + M^2}$  to fit the data.  $J_{\text{shunt}}$  is Johnson noise in the shunt resistor.  $P_{\text{bath}}$  is the theoretical thermal fluctuation noise between TES and thermal bath. This term was increased by 30% in panel (a) and 45% in panel (b) when calculating the total noise to obtain a good fit to the data at low frequency. Readout noise is the noise level measured in the superconducting state from readout components, which is assumed to be white. The difference in the readout noise between the hydra and single-pixel is a consequence of different SQUID readout chips being used for each measurement. All noise terms include the high frequency roll-off from readout electronics.

warrants further study, and in particular, the apparent difference in magnitude between the hydra and single-pixel is an interesting avenue to pursue.

### 3.2.2 Pulse-shape

The pulse-shape from  $C K_\alpha$  x-rays is shown in Fig. 8 for the single-pixel and for each of the four pixels of the hydra. The hydra pulse-shapes for the different absorbers are distinguished by their different rise-times. The model used to fit the measured noise in Fig. 7 has also been used to predict the small-signal pulse-shape, as shown in Fig. 8. In the single-pixel, we observe reasonable agreement between the modeled and measured pulse-shape. There is good agreement between the time constants of the pulse and only a small discrepancy in pulse height of  $\sim 10\%$ . In general, the agreement is also good in the hydra design, with the fall-times of the modeled pulse and the separation of the pulse-shapes of the four pixels well described. Looking in detail, it is clear that in the fastest pulse from pixel 1, the predicted pulse-shape is slightly different at the peak, and there is a discrepancy in the predicted and measured

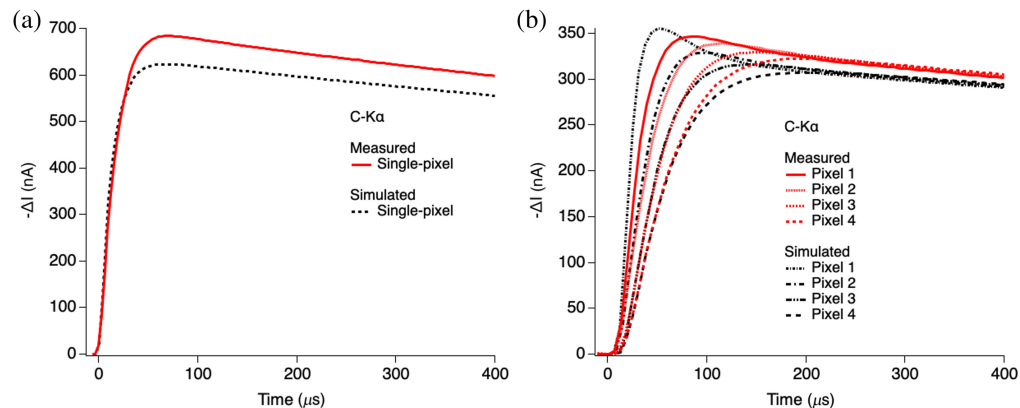


**Fig. 8** Measured TES current pulse-shape (red) from  $C K_\alpha$  x-rays compared with the predicted pulse-shape (black) for (a) single-pixels and (b) hydra. Pulse-shape is predicted using the model described in Secs. 2.2 and 3.2.1. Data were taken at  $R/R_n = 10\%$  and  $T_{\text{bath}} = 40$  mK.

rise-time of  $\sim 40\%$ . This discrepancy is found to get larger at higher energies and is, therefore, likely a consequence of non-linearity of the TES response as it leaves the small-signal limit used in the model.

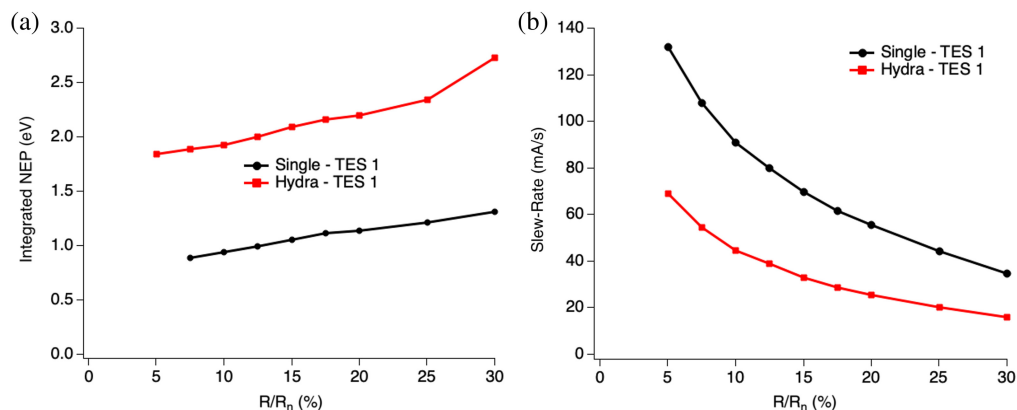
### 3.2.3 Integrated noise equivalent power

The integrated noise equivalent power (NEP) for a TES microcalorimeter is an estimate of the achievable energy resolution of the device based on the measured detector responsivity and the measured noise at the equilibrium bias point before an x-ray event.<sup>3,35,36</sup> Figure 9(a) shows the integrated NEP of the single-pixel and hydra as a function of  $R/R_n$  for the Al  $K_\alpha$  x-rays. This shows that the integrated NEP increases as the bias point resistance increases. At  $R/R_n = 10\%$ , the integrated NEP in the single-pixel is 0.94 eV, and the average integrated NEP in the hydra is 1.93 eV. The integrated NEP in the four pixels in the hydra ranges from 1.91 to 1.94 eV.

In the hydra, the integrated NEP is approximately a factor of two larger than that in the single-pixel. The energy resolution of a TES microcalorimeter is predicted to be proportional to  $\sqrt{C_{\text{tot}}}$ , where  $C_{\text{tot}}$  is the total heat capacity. Therefore, although there are additional noise terms in the hydra pixels compared with the single-pixel, the increase in the integrated NEP in the hydra is consistent with the factor of approximately four increase in the total heat capacity. This is in agreement with the small contribution of the fitted thermal fluctuation noise between the TES and the four absorbers shown in Fig. 7, and it shows that there is little additional degradation in the integrated NEP as a result of the hydra design, as expected.

### 3.2.4 Slew-rate

The slew-rate is defined as the maximum in the time derivative of the current through the TES during an x-ray pulse. This is a key performance metric for the design of the LMS because the slew-rate for the maximum incident energy will determine the minimum TDM readout noise that can be achieved in a stable system and therefore the maximum multiplexing factor that can be achieved for a given energy resolution requirement.<sup>21,37</sup> Figure 9(b) shows the slew-rate during an Al  $K_\alpha$  x-ray pulse, as a function of  $R/R_n$  for the single-pixel and pixel 1 of the hydra, which has the highest slew-rate of the four pixels. The figure shows that the slew-rate decreases with higher bias point resistance and is larger in the single-pixel than the hydra. This difference is largely because of the increased heat capacity in the hydra from the four absorbers, but the difference in added inductance  $L$  and critical inductance  $L_{\text{crit}}$  in the two circuits also influences the slew-rate difference. For the single-pixel with a circuit inductance of 640 nH ( $L/L_{\text{crit}} = 0.14$ ), this gives 91 mA/s at 10%  $R_n$ , and in the hydra with a circuit inductance of 1370 nH ( $L/L_{\text{crit}} = 0.22$ ), the slew-rate was 44 mA/s for pixel 1 at 10%  $R_n$ .



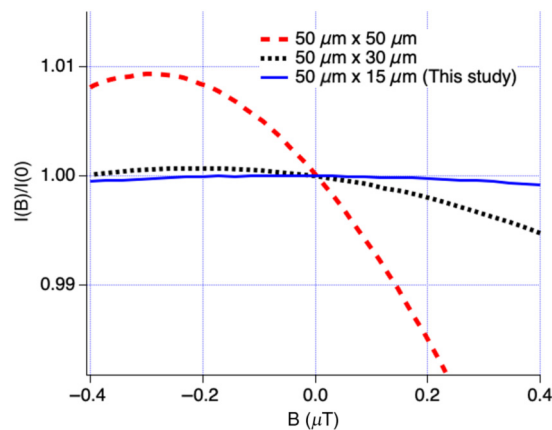
**Fig. 9** Measured data for hydra and single-pixels showing (a) integrated NEP for Al  $K_\alpha$  x-rays as a function of  $R/R_n$ . Integrated NEP for the hydra is the average of the four pixels. (b) Measured slew-rate, the maximum in the time-derivative of TES current, during an Al  $K_\alpha$  x-ray pulse as a function of  $R/R_n$ . The slew-rate in the hydra is for pixel 1, which is the highest of the four.

Figure 9 suggests that, although the integrated NEP is improved by going to bias points that are lower in the transition, and therefore the energy resolution might also be improved, this will lead to an increase in the slew-rate. When optimizing for TDM readout, the larger slew-rate means a larger noise contribution to the energy resolution when using multiplexed readout for a fixed number of TDM rows and energy range.<sup>37</sup> Therefore, for the LEM mission, the bias point must be carefully chosen to optimize the system within these constraints.<sup>22,23</sup> Here, we continue to focus on the behavior at  $R/R_n = 10\%$  as a well optimized point, but small improvements in overall performance may be possible in the future through minor adjustments to this value.

### 3.2.5 Energy gain scale sensitivity

The energy gain scale is an empirical function that is used to determine the energy deposited in the microcalorimeter, in units of eV, from the optimally filtered pulse height measured in the TES from this event.<sup>20,38</sup> An important parameter for any TES microcalorimeter instrument is the sensitivity of this energy gain scale to external perturbations such as magnetic field, bath temperature, or TES bias voltage. These appear as noise terms in the instrument energy resolution budget, and the minimization of these terms can have a significant impact on the instrument design. In particular, the sensitivity of the energy gain scale to variations in magnetic field perpendicular to the plane of the TES has been a key parameter in the design for X-IFU<sup>27,39,40</sup> and will be important in the design of LEM.

To investigate this gain sensitivity to magnetic field, we first measured the TES current as a function of magnetic field perpendicular to the plane of the TES  $I(B)$ . Figure 10 shows  $I(B)$  normalized by dividing by  $I(B = 0)$  for the single-pixel measured in this work, as well as previously reported data on single-pixel TESs with larger widths.<sup>27</sup> All of the data were taken with a constant voltage bias applied for each design to give  $R/R_n = 10\%$  at  $B = 0$ . The previous data on pixels optimized for the X-IFU instrument were measured with a bath temperature of 55 mK, and the  $50 \mu\text{m} \times 15 \mu\text{m}$  TES studied here was measured at  $T_{\text{bath}} = 40 \text{ mK}$ . These data show that reducing the TES width to  $15 \mu\text{m}$  leads to a further reduction in  $(dI/dB)/I(0)$  compared with a width of  $30 \mu\text{m}$ . This is expected; as the effective area of the weak-link is reduced, the current distribution across the TES is altered, and the effect of self-field from the TES current is also reduced.<sup>14,27,36,41,42</sup> The reduced sensitivity of the TES current to magnetic field in narrower devices correlates with a reduced gain scale sensitivity of the x-ray pulse height to variations in the magnetic field. This magnetic field dependence is calculated as the change in the energy gain scale at 1.5 keV  $\delta E_B$ , after optimal filtering, divided by the change in magnetic field  $B$ . This value is shown for each pixel type in Table 1 and is more than an order of magnitude smaller than



**Fig. 10** TES current  $I$  as a function of magnetic field  $B$  divided by  $I(B = 0)$  measured on the single-pixel TES from this study with a length  $\times$  width of  $50 \mu\text{m} \times 15 \mu\text{m}$ . This is compared with previous measurements of TESs studied for X-IFU with a length  $\times$  width of  $50 \mu\text{m} \times 50 \mu\text{m}$  and  $50 \mu\text{m} \times 30 \mu\text{m}$  for TES.<sup>27</sup> Thermal bath temperature  $T_{\text{bath}}$  was at 40 mK for the  $50 \mu\text{m} \times 15 \mu\text{m}$  TES and 55 mK for the others. Each TES was biased with a constant voltage such that  $R/R_n = 10\%$  at  $B = 0$ .

**Table 1** Sensitivity of the energy gain scale to environmental conditions for the hydra and single-pixel when biased at  $R/R_n = 10\%$ .

	Single-pixel	Hydra
$\delta E/dT_{\text{bath}}$ (meV/ $\mu\text{K}$ )	77.5	79
$\delta E/dB$ (meV/nT)	3.9	6.7
$V_{\text{bias}}\delta E/dV_{\text{bias}}$ (meV/ppm)	1.7	1.8

$\sim 200$  meV/nT measured at 6 keV in the  $50 \mu\text{m} \times 30 \mu\text{m}$  TES proposed as a potential new baseline for X-IFU.<sup>27</sup>

The table also includes the measured sensitivity of the energy gain scale to variation in the bath temperature and TES voltage bias at 1.5 keV.

### 3.2.6 Energy resolution

The energy resolution of the single and hydra pixels was measured for the  $\text{Al K}\alpha_{1,2}$  line at  $R/R_n = 10\%$  and a bath temperature of 40 mK. The fitted spectra are shown in Fig. 11. Figure 11(b) shows the coadded spectrum for the four absorbers of the hydra. The spectral resolution of each pixel in the hydra from 1 to 4 was  $1.90 \pm 0.04$ ,  $1.93 \pm 0.04$ ,  $1.92 \pm 0.04$ , and  $1.92 \pm 0.04$  eV. All of these spectral resolution measurements are in agreement with the integrated NEP.

### 3.3 Position Sensitivity in Time-Division Multiplexed Readout

Readout of the  $\sim 4000$  TESs on LEM will use TDM to reduce the number of readout channels required. Full performance testing of the LEM pixels with TDM will require the fabrication of SQUID readout chips optimized for these pixel designs. This optimization of the readout is described elsewhere.<sup>22,23</sup> Here, we limited our TDM measurements to testing a key feature of the hydra pixel design, which is whether there is sufficient position sensitivity between the four pixels of the hydra over the targeted energy range when the x-ray pulses are sampled at the rate expected in LEM. To do this, we measured four 4-pixel hydras using TDM readout. The readout used 10 timing rows to read out these four physical TESs and six “dummy” rows. The sample rate was 102.4 kHz, which is within a few percent of the expected sample rate on LEM of 104.17 kHz. The pixels were then illuminated with an x-ray source with a range of characteristic lines from  $\sim 0.3$  to  $\sim 2$  keV and Bremsstrahlung radiation up to  $\sim 4$  keV.

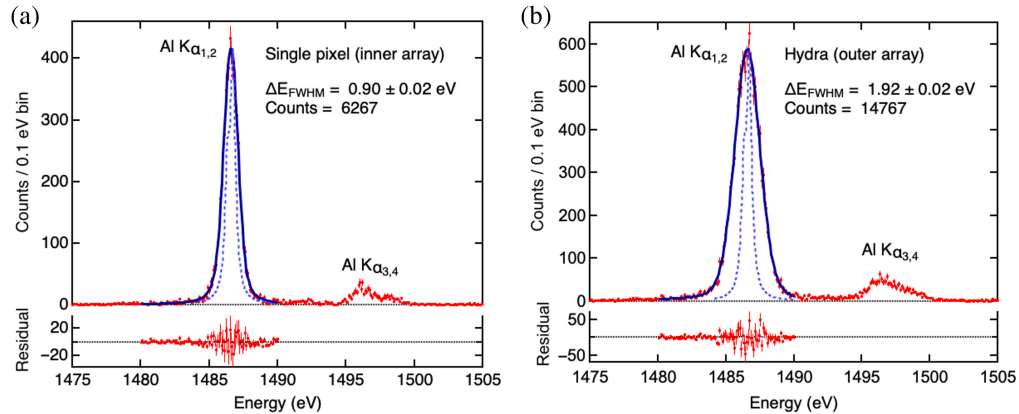


**Fig. 11** Fitted energy resolution for the  $\text{Al K}\alpha_{1,2}$  line for (a) the single-pixel and (b) the coadded spectrum of the 4 pixels of the hydra. Red dots are the measured energy histogram, the blue dashed line is the assumed natural line shape of the  $\text{Al K}\alpha$  complex from literature, and the solid black line is the fit to the measured data. Data were measured at  $T_{\text{bath}} = 40$  mK and  $R/R_n = 10\%$ .

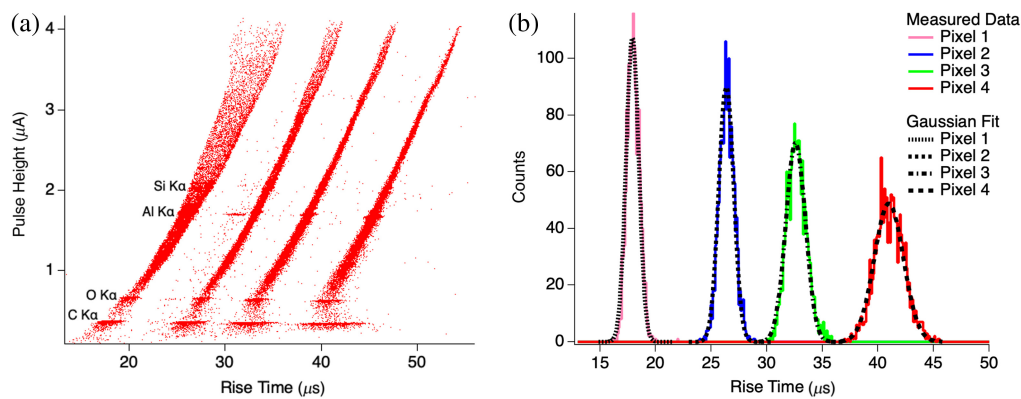


**Fig. 12** (a) Pulse height in the hydra TES current as a function of pulse rise time when illuminated with a broad band source. (b) Measured (solid) distribution of the rise time for the four pixels at the C  $K_{\alpha}$  line and a Gaussian fit (dashed) to each distribution.

Figure 12(a) shows the pulse height of the x-ray pulse as a function of the pulse rise time, where rise time is defined as the time taken for the current to rise from 20% to 80% of the pulse height and divided by  $(\ln 0.8 - \ln 0.2)$  to convert to an equivalent exponential time constant. In this parameter-space, the four pixels of the hydra are clearly distinguishable as four separate bands, as expected. The sample rate of the pulse measurement is a key parameter because, at a given energy, as the sample rate is reduced, the variation in the measured rise time increases and could potentially prevent position discrimination. However, in these pixels, at the sample rate required for LEM, each pixel is well separated.

The spread in the rise time is also a function of the x-ray energy  $E$ , with the full width half maximum of the rise time distribution expected to increase at lower energies proportional to  $1/E$  for pulses that are sufficiently sampled.<sup>43</sup> Figure 12(b) shows the distribution of measured rise times for the C  $K_{\alpha}$  line across the four pixels of the hydra. This shows that, even at this low energy, the pixels are clearly distinguishable. Fitting a Gaussian curve to each of these distributions, we are able to estimate the probability of a C  $K_{\alpha}$  x-ray being measured in a region of overlap between two pixels as  $<0.1\%$ .

Note that the approximate white noise from the TDM readout during the measurement shown in Fig. 12 was  $\sim 5 \text{ pA}/\sqrt{\text{Hz}}$ . This is less than the  $12 \text{ pA}/\sqrt{\text{Hz}}$  baselined for LEM,<sup>22,23</sup> and increased TES noise will increase the width of the rise time distributions. This will have the largest impact at low energies where the signal-to-noise is smallest. The effect of this small increase in white noise was simulated by adding random white noise to the measured data. This simulation showed that, even with the added noise, the overlap between the Gaussian distributions of the four pixels is predicted to be  $\sim 0.1\%$  at the C  $K_{\alpha}$  line. Extrapolating these results to the lowest energy for the LEM mission of 200 eV, using the  $1/E$  scaling discussed above, we estimate an overlap of 3.1%. This overlap of a few percent is anticipated to be acceptable for the LEM mission, but full simulations will need to be completed before a requirement can be set. Note that we do not expect electrical cross-talk to impact position discrimination.

There is an additional feature observable in the plot of pulse height as a function of rise time shown in Fig. 12(a). At the Al  $K_{\alpha}$  line, which is the line with the most events, there are a small number of events between the bands of the first and second pixels. The number of events in this region is  $\sim 0.1\%$  of the total Al  $K_{\alpha}$  events seen in the four pixels. This fraction is approximately equal to the area of the TES that is exposed between the four absorbers, divided by the total area of the four absorbers. Therefore, we postulate that these events arise from the absorption of X-rays directly in the TES. In the small-signal limit, these events are predicted to have pulse-shapes very similar to events in pixel 1 and would likely be indistinguishable here. However, the effects of non-linearity of the TES response will affect pulses from events in pixel 1 differently than those in the TES and therefore may explain this apparent discrepancy. Very high statistics spectra over a wide range of incident energies will be performed in future work to confirm whether this feature is indeed from x-ray absorption directly in the TES.

## 4 Discussion

The comprehensive results presented in Sec. 3 demonstrate that these hydra and single-pixel designs have excellent characteristics that are well suited to implementation in the LMS on LEM. The resistive transitions of these  $50\ \mu\text{m} \times 15\ \mu\text{m}$  TESs are a smooth function without discontinuities, as expected for devices without normal metal bars perpendicular to the current direction in the TES.<sup>14</sup> In this chip, the  $\alpha$  is smaller and  $\beta$  is larger at  $R/R_n = 10\%$  than has been seen in other  $50\ \mu\text{m}$  long TESs.<sup>10,27</sup> The intrinsic bilayer transition temperature in these TESs is significantly lower than those measured before, which may have an impact. However, in general, the lower  $\alpha/\beta$  observed here is consistent with evidence presented elsewhere that the transition parameters may predominantly be sensitive to the sheet resistance of the bilayer, rather than the TES width or  $T_c$ .<sup>27</sup> This apparent correlation warrants further study. In the future, by fine-tuning the bilayer sheet resistance, there may be potential to adjust parameters and further optimize the instrument's performance.

The measurements and modeling of the noise and pulse-shapes in the hydra and single-pixels indicate that the performance of these is generally well understood. In addition to adjustments to the TES bilayer mentioned above, small improvements to the performance may be possible through slight adjustments of  $C_a$ ,  $L$ , and the chosen resistive bias point. These adjustments, as well as further investigation of the excess phonon and Johnson noise, will be the subject of future studies. However, the performance of the devices studied here is already excellent. At  $R/R_n = 10\%$ , the integrated NEP of the single-pixels and the average of the hydra pixels is 0.94 eV and 1.93 eV, respectively. The spectral resolution at 1.5 keV was found to be in agreement with these values. The instrument energy resolution requirement is 1.3 eV and 2.5 eV for the single-pixel and hydra, respectively. Therefore, there is a significant margin on the requirement for additional error terms at the instrument level, such as the contribution of the multiplexed readout and environmental perturbations. The measured slew-rate of the x-ray pulses provides input on the multiplexing factor that can be achieved on LEM using TDM. This optimization is discussed in detail elsewhere, but it is estimated that the target of 60 row multiplexing will be achievable.<sup>22,23</sup> The degradation of energy resolution with environmental perturbations is dependent on the sensitivity of the energy gain scale to these perturbations. The measurements of the sensitivities to  $T_{\text{bath}}$ ,  $B$ , and  $V_{\text{bias}}$  shown in Table 1 are in reasonable agreement with expectations based on extrapolation from data on other devices.<sup>10</sup> It is noteworthy that  $\delta E/dB$  is found to be over two orders of magnitude smaller than the devices currently baselined for use on X-IFU because of the narrower width of the TES in LEM. These gain sensitivities provide input for the instrument design and the instrument energy resolution budget.<sup>22</sup>

The detector performance under TDM will need to be verified using TDM readout components optimized for these devices, with representative values of  $R_{\text{shunt}}$ ,  $L$ , and noise levels, as well as timings consistent with the requirements for LEM. However, we were able to show in Sec. 3.3 that, under TDM readout with representative timing, full position sensitivity of the four pixels of the hydra was achievable down to energies of 200 eV. This is crucial evidence that this multi-absorber TES design is suitable for LEM and other future astrophysics applications.

## 5 Conclusion

In conclusion, we have presented the first characterization of a hybrid array of single and multi-absorber TES microcalorimeters designed for the proposed LEM mission. The spectral resolution for the  $\text{AlK}\alpha$  line was found to be  $1.92 \pm 0.02$  eV for the 4-pixel hydra (coadded) and  $0.90 \pm 0.02$  eV for the single-pixels. Detailed studies of the transition, pulse, and gain scale sensitivity properties all indicate excellent suitability for the mission and will provide input to the LMS design and the instrument energy resolution budget. Measurements were performed of the position sensitivity of a hydra under TDM with row timings representative of that proposed for LEM. This showed that discrimination between the four pixels was achievable down to energies of 200 eV.

---

### Code, Data, and Materials Availability

The data presented here are available from the authors upon request.

## Acknowledgments

The material is based upon work supported by NASA (Grant No. 80GSFC21M0002).

## References

1. R. Kraft et al., “Line emission mapper (LEM): probing the physics of cosmic ecosystems,” arXiv:2211.09827 (2023).
2. S. J. Smith et al., “Development of position-sensitive transition-edge sensor x-ray detectors,” *IEEE Trans. Appl. Supercond.* **19**(3), 451–455 (2009).
3. S. J. Smith et al., “Toward 100,000-pixel microcalorimeter arrays using multi-absorber transition-edge sensors,” *J. Low Temp. Phys.* **199**, 330–338 (2020).
4. J. N. Ullom and D. A. Bennett, “Review of superconducting transition-edge sensors for x-ray and gamma-ray spectroscopy\*,” *Supercond. Sci. Technol.* **28**, 084003 (2015).
5. L. Gottardi and S. Smith, “Transition-edge sensors for cryogenic x-ray imaging spectrometers,” in *Handbook of X-ray and Gamma-ray Astrophysics*, C. Bambi and A. Santangelo, Eds., pp. 1–46, Springer Nature, Singapore (2022).
6. S. R. Bandler et al., “Lynx x-ray microcalorimeter,” *J. Astron. Telesc. Instrum. Syst.* **5**(2), 021017 (2019).
7. A. E. Hornschemeier, N. E. White, and H. Tananbaum, “The frontier in x-ray spectroscopy: NASA’s constellation-X mission,” *AIP Conf. Proc.* **774**, 383–389 (2005).
8. S. J. Smith et al., “Development of arrays of position-sensitive microcalorimeters for Constellation-X,” *Proc. SPIE* **7011**, 701126 (2008).
9. D. Barret et al., “The Athena x-ray integral field unit: a consolidated design for the system requirement review of the preliminary definition phase,” *Exp. Astron.* **55**(2), 373–426 (2023).
10. K. Sakai et al., “Demonstration of a full-scale brassboard tes microcalorimeter array for the athena X-IFU,” *IEEE Trans. Appl. Supercond.* **33**(5), 1–5 (2023).
11. S. J. Smith et al., “Performance of a broad-band, high-resolution, transition-edge sensor spectrometer for x-ray astrophysics,” *IEEE Trans. Appl. Supercond.* **31**(5), 1–6 (2021).
12. M. Durkin et al., “Demonstration of athena X-IFU compatible 40-row time-division-multiplexed readout,” *IEEE Trans. Appl. Supercond.* **29**(5), 1–5 (2019).
13. K. Nagayoshi et al., “Development of a Ti/Au TES microcalorimeter array as a backup sensor for the Athena/X-IFU instrument,” *J. Low Temp. Phys.* **199**, 943–948 (2020).
14. N. Wakeham et al., “Effects of normal metal features on superconducting transition-edge sensors,” *J. Low Temp. Phys.* **193**, 231–240 (2018).
15. K. M. Morgan et al., “Dependence of transition width on current and critical current in transition-edge sensors,” *Appl. Phys. Lett.* **110**, 212602 (2017).
16. K. Nagayoshi et al., “Lateral inverse proximity effect in Ti/Au transition edge sensors,” *J. Low Temp. Phys.* **209**, 540–547 (2022).
17. N. A. Wakeham et al., “Thermal fluctuation noise in Mo/Au superconducting transition-edge sensor microcalorimeters,” *J. Appl. Phys.* **125**, 164503 (2019).
18. A. Wessels et al., “A model for excess Johnson noise in superconducting transition-edge sensors,” *Appl. Phys. Lett.* **118**, 202601 (2021).
19. L. Gottardi et al., “Voltage fluctuations in AC biased superconducting transition-edge sensors,” *Phys. Rev. Lett.* **126**, 217001 (2021).
20. S. J. Smith et al., “Correcting gain drift in TES detectors for future x-ray satellite missions,” *IEEE Trans. Appl. Supercond.* **33**(5), 1–6 (2023).
21. W. B. Doriese et al., “Optimization of time- and code-division-multiplexed readout for Athena X-IFU,” *IEEE Trans. Appl. Supercond.* **29**(5), 1–5 (2019).
22. S. J. Smith et al., “Development of the microcalorimeter and anti-coincidence detector for the Line Emission Mapper x-ray probe,” *J. Astron. Telesc. Instrum. Syst.* **9**(4), 041005 (2023).
23. S. R. Bandler et al., “The Line Emission Mapper microcalorimeter spectrometer,” *J. Astron. Telesc. Instrum. Syst.* **9**(4), 041002 (2023).
24. C. Bailey et al., “Implications of weak link effects on thermal characteristics of transition-edge sensors,” *J. Low Temp. Phys.* **167**, 121–128 (2012).
25. S. Lee et al., “Fine pitch transition-edge sensor x-ray microcalorimeters with sub-EV energy resolution at 1.5 keV,” *Appl. Phys. Lett.* **107**(22), 223503 (2015).
26. M. de Wit et al., “High aspect ratio transition edge sensors for x-ray spectrometry,” *J. Appl. Phys.* **128**, 224501 (2020).
27. N. A. Wakeham et al., “Refinement of transition-edge sensor dimensions for the x-ray integral field unit on Athena,” *IEEE Trans. Appl. Supercond.* **33**(5), 1–6 (2023).
28. H. F. C. Hoervers et al., “Radiative ballistic phonon transport in silicon-nitride membranes at low temperatures,” *Appl. Phys. Lett.* **86**, 251903 (2005).

29. E. Taralli et al., “Performance and uniformity of a kilo-pixel array of Ti/Au transition-edge sensor microcalorimeters,” *Rev. Sci. Instrum.* **92**, 023101 (2021).
30. M. A. Lindeman et al., “Impedance measurements and modeling of a transition-edge-sensor calorimeter,” *Rev. Sci. Instrum.* **75**, 1283–1289 (2004).
31. E. Figueroa-Feliciano, “Complex microcalorimeter models and their application to position-sensitive detectors,” *J. Appl. Phys.* **99**, 114513 (2006).
32. N. Wakeham et al., “High-frequency noise peaks in mo/au superconducting transition-edge sensor microcalorimeters,” *J. Low Temp. Phys.* **200**, 192–199 (2020).
33. A. R. Miniussi et al., “Performance of an x-ray microcalorimeter with a 240  $\mu\text{m}$  absorber and a 50  $\mu\text{m}$  tes bilayer,” *J. Low Temp. Phys.* **193**, 337–343 (2018).
34. M. E. Eckart et al., “Large-absorber TES X-ray microcalorimeters and the micro-X detector array,” *AIP Conf. Proc.* **1185**, 699–702 (2009).
35. K. Irwin and G. Hilton, *Transition-Edge Sensors*, pp. 63–150, Springer Berlin Heidelberg, Berlin, Heidelberg (2005).
36. S. J. Smith et al., “Implications of weak-link behavior on the performance of Mo/Au bilayer transition-edge sensors,” *J. Appl. Phys.* **114**, 074513 (2013).
37. W. Doriese et al., “Optimization of the TES-bias circuit for a multiplexed microcalorimeter array,” *J. Low Temp. Phys.* **167**, 595–601 (2012).
38. J. W. Fowler et al., “The practice of pulse processing,” *J. Low Temp. Phys.* **184**, 374–381 (2016).
39. A. Bergen et al., “Design and validation of a large-format transition edge sensor array magnetic shielding system for space application,” *Rev. Sci. Instrum.* **87**, 105109 (2016).
40. D. Vaccaro et al., “Susceptibility study of tes micro-calorimeters for x-ray spectroscopy under fdm readout,” *J. Low Temp. Phys.* **209**(3–4), 562–569 (2022).
41. J. E. Sadleir, “Superconducting transition-edge sensor physics,” PhD thesis, University of Illinois (2011).
42. M. de Wit et al., “Performance of the SRON Ti/Au transition edge sensor x-ray calorimeters,” *Proc. SPIE* **12181**, 121812B (2022).
43. S. J. Smith, C. H. Whitford, and G. W. Fraser, “Optimised filtering for improved energy and position resolution in position-sensitive tes based x-ray detectors,” *Nucl. Instrum. Methods Phys. Res. Sect. A Accel. Spectrom. Detect. Assoc. Equip.* **556**(1), 237–245 (2006).

**Nicholas Wakeham** is an assistant research scientist at the University of Maryland Baltimore County working at the NASA Goddard Space Flight Center. He received his PhD in low temperature condensed matter physics from the University of Bristol in 2013 and was a postdoctoral researcher at Los Alamos National Laboratory from 2013 until he became a NASA Postdoctoral Fellow at GSFC in 2016. His interests are exotic electronic states, unconventional superconductivity, and superconducting detectors.

**Simon R. Bandler** is a research astrophysicist at NASA’s Goddard Space Flight Center. He received his BS degree in mathematical physics from the University of Sussex in the United Kingdom and his MS degree and PhD in physics from Brown University in 1992 and 1996, respectively. He is the author of more than 200 journal papers. His current research interests include transition-edge sensor and magnetic x-ray microcalorimeters, x-ray astrophysics, and the ESA flagship mission called Athena.

**Stephen J. Smith** is a research astrophysicist at NASA Goddard Space Flight Center. He received his MPhys degree in physics with space science and technology in 2002 and his PhD in physics in 2006, both from the University of Leicester, United Kingdom. He is an author of more than 150 published papers. His primary research interests are in the development of cryogenic detectors for x-ray astronomy applications.

Biographies of the other authors are not available.